Pathak, S., Ibele, L. M., Boll, R., Callegari, C., Demidovich, A., Erk, B., Feifel, R., Forbes, R., Di Fraia, M., Giannessi, L., Hansen, C. S., Holland, D. M. P., Ingle, R. A., Mason, R., Plekan, O., Prince, K. C., Rouzée, A., Squibb, R. J., Tross, J., ... Rolles, D. (2020). Tracking the Ultraviolet Photochemistry of Thiophenone During and After the Initial Ultrafast Ring Opening. *Nature Chemistry*, *12*, 795-800. https://doi.org/10.1038/s41557-020-0507-3

Peer reviewed version

Link to published version (if available):
10.1038/s41557-020-0507-3

Supplementary Information

Tracking the ultraviolet-induced photochemistry of thiophenone during and after ultrafast ring opening

Shashank Pathak[1+], Lea M. Ibele[2+], Rebecca Boll[3], Carlo Callegari[4], Alexander Demidovich[4], Benjamin Erk[5], Raimund Feifel[6], Ruaridh Forbes[7], Michele Di Fraia[4], Luca Giannessi[4,8], Christopher S. Hansen[9], David M.P. Holland[10], Rebecca A. Ingle[11], Robert Mason[12], Oksana Plekan[4], Kevin C. Prince[4,13], Arnaud Rouzée[14], Richard J. Squibb[6], Jan Tross[1], Michael N.R. Ashfold[15*], Basile F.E. Curchod[2*], and Daniel Rolles[1*]

[+]*both authors have contributed equally*
[*]*corresponding authors*

[1]*J.R. Macdonald Laboratory, Department of Physics, Kansas State University, Manhattan, KS, USA*
[2]*Department of Chemistry, Durham University, Durham DH1 3LE, UK*
[3]*European XFEL, Schenefeld, Germany*
[4]*Elettra - Sincrotrone Trieste S.C.p.A., 34149 Basovizza, Trieste, Italy*
[5]*Deutsches Elektronen-Synchrotron, 22607 Hamburg, Germany*
[6]*Department of Physics, University of Gothenburg, Gothenburg, Sweden*
[7]*Stanford PULSE Institute, SLAC National Accelerator Laboratory, Menlo Park, CA 94025, USA*
[8]*Istituto Nazionale di Fisica Nucleare, Laboratori Nazionali di Frascati, 00044 Frascati (Rome), Italy*
[9]*School of Chemistry, University of New South Wales, Sydney NSW 2052, Australia*
[10]*Daresbury Laboratory, Daresbury, Warrington, Cheshire WA4 4AD, UK*
[11] *Department of Chemistry, University College London, London, WC1H 0AJ, UK*
[12]*Department of Chemistry, University of Oxford, Oxford, OX1 3TA, UK*
[13]*Centre for Translational Atomaterials, Swinburne University of Technology, Melbourne, Australia*
[14]*Max-Born-Institut, 12489 Berlin, Germany*
[15]*School of Chemistry, University of Bristol, Bristol, BS8 1TS, UK*

Table of Contents:

1. *Experimental details*

2(5H)-thiophenone (Sigma Aldrich, 98%) seeded in a helium carrier gas at 2 bar backing pressure was introduced into the vacuum chamber through a pulsed Even-Lavie valve heated to 60 ºC. The FEL pulses were focused to a spot of 40 x 50 μm^2 (FWHM) and had an average pulse energy of 18 μJ (measured before the beamline optics). The calculated transmission of the transport optics at this wavelength is 0.27 [*Svetina2015*], implying an average pulse energy of 4.9 μJ at the sample. The UV pump pulses (center wavelength: 264.75 nm, bandwidth: 1.2 nm) were generated as the third harmonic of a Ti:Sapphire laser and had an average pulse energy of 25 μJ, focused to a diameter of ~200 μm (FWHM). To investigate the dependence of the observed effects on the pulse energy of the pump and probe pulses, delay scans were taken at several lower and higher pulse energies (see Fig. 4). The observed spectral components and time scales were found to be independent of the pulse energies.

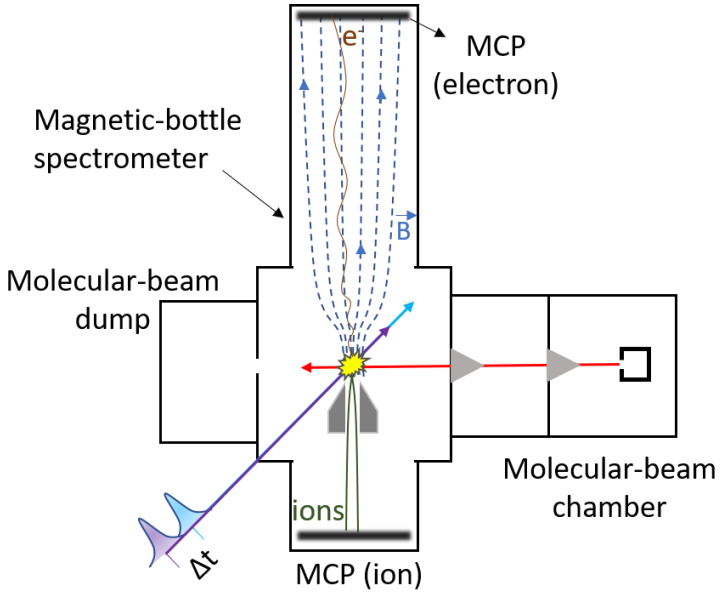

Figure 1: Schematic of experimental setup. The FEL and UV pulses intersect a cold beam of target molecules seeded in helium carrier gas that is introduced into the vacuum chamber by supersonic expansion through a pulsed valve. Photoelectrons created by the interaction of the FEL pulses with the target are guided onto an MCP detector by the electric and magnetic (**B**) field of the magnetic bottle spectrometer. Photoions, although not discussed further in this work, are extracted through a hole in the magnet of the magnetic bottle and are detected on a second MCP detector opposite to the electron detector.

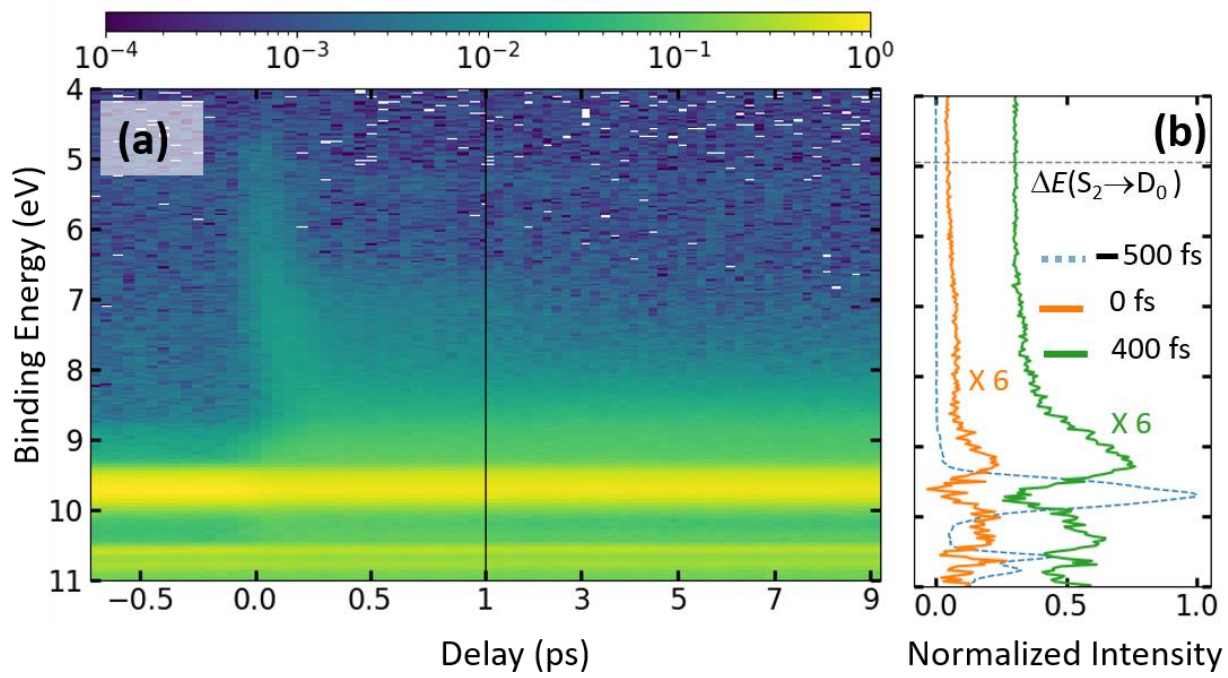

Figure 2: Measured photoelectron yield as a function of binding energy and pump-probe delay. Note the different scaling of the delay axis below and above Δt = 1 ps, and the larger binding energy range and different color scale than used in Fig. 2(a) of the main text. The strong contributions at BE ~9.7 and BE ~10.6 eV correspond to ionization to the D_0/D_1 and the D_2 states of the cation, respectively [*Chin1998*]. Photoelectrons with BE >11 eV were not detected because a retardation voltage of 8 V was used to obtain better resolution for the electrons with lower binding energies. (b) Photoelectron spectra for the FEL pulse preceding the UV pulse (Δt = –500 fs, dashed blue line) and at two delays where the UV pulse precedes the FEL pulse (orange: Δt = 0; green: Δt = 400 fs; each scaled by a factor of 6 and offset by, respectively, 0.04 and 0.3 for better visibility). For the latter two, the contributions from 'unpumped' molecules have been subtracted (see Fig. 3), and the data are integrated over a range of ±40 fs around the indicated Δt value. The ionization potential for vertical ionization (in the ground-state equilibrium geometry) from the S_2 excited state to the D_0 state of the cation (taken from [*Chin1998*]) is shown as a dashed line.

Table 1: Least-square fits of the delay-dependent photoelectron yields. Fit parameters obtained from least-square fits to the lineouts of the photoelectron yield in selected binding energy ranges shown in Fig. 2(b) of the main text. The data are fitted by a Gaussian (G(x)), the convolution C(x) = (f*h)(x) of a Gaussian (h(x)) with an exponential decay (f(x)); or by a cumulative distribution function (CDF(x)), as appropriate and as defined below.

Energy Range	**Fit Function**	**x_0/fs**	**σ/fs**	**τ/fs**
(4.7 – 5.3) eV	Gaussian	4 ± 5	76 ± 6	-
(8.3 – 9.1) eV	Gaussian * Exponential	-2 ± 7	75 (fixed)	72 ± 9
(9.5 – 9.9) eV	CDF	-15 ± 5	72 ± 8	-

$$G(x) = Ae^{\frac{-(x-x_0)^2}{2\sigma^2}} + y_0$$

$$CDF(x) = \frac{A}{2}\left(1 + \text{erf}\left(\frac{x - x_0}{\sqrt{2\sigma^2}}\right)\right) + B$$

Convolution of Gaussian $h(x) = e^{-\frac{x^2}{2\sigma^2}}$ and

exponential (for x> x0) $f(x) = \text{Heaviside}(x - x0)\left\{\left(1 - e^{\frac{-(x-x0)}{\tau}}\right) + b\right\}$:

$$C(x) = \sigma e^{-\frac{x}{\tau}}\sqrt{\frac{\pi}{2}}\left((a+b)e^{\frac{x}{\tau}}\left(1 + \text{Erf}\left[\frac{x}{\sigma\sqrt{2}}\right]\right) - ae^{\frac{2\tau x0+\sigma^2}{2\tau^2}}\text{Erfc}\left[\frac{(-\tau x+\sigma^2)}{\sigma\sqrt{2}\tau}\right]\right)$$

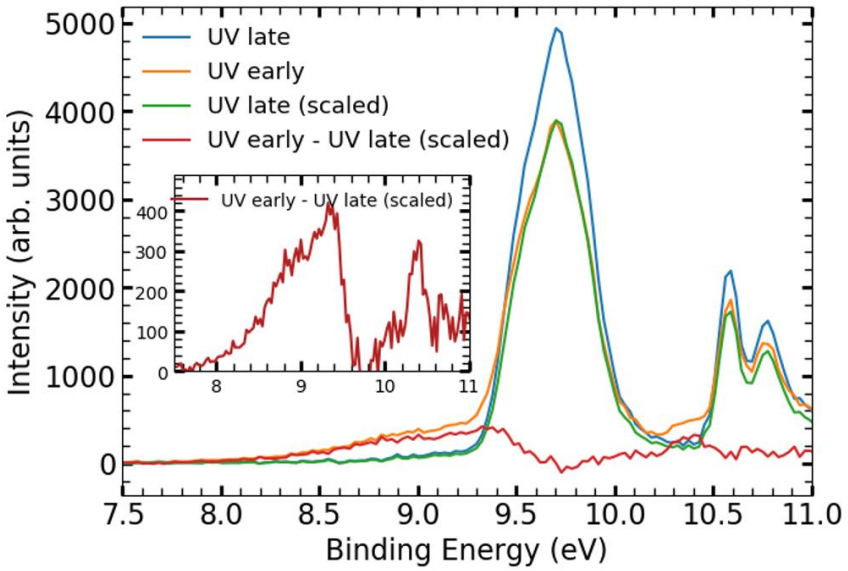

Figure 3: Subtraction of signal from 'unpumped' molecules. To isolate the time-dependent signal stemming from photoexcited molecules, the photoelectron spectrum measured at negative Δt (*i.e.* FEL pulse arriving before the UV pulse, blue curve, 'UV late') is used in order to subtract the signal from unpumped molecules at positive delays (orange curve, 'UV early'). For delays Δt >0.2 ps, the fraction of unpumped molecules is constant, and a constant scaling factor is chosen. However, in the temporal overlap region, the subtraction procedure needs to recognize the gradual decrease of this signal caused by the increasing ground-state depletion. To determine the appropriate scaling factor for a given delay, the 'UV late' spectrum is scaled such that it has the same photoelectron yield in the binding energy range between 9.5 and 9.9 eV as the spectrum at the given delay. This procedure is repeated for all delay points in the overlap region, and a cumulative distribution function (CDF) is fitted to obtain a smooth scaling function that is used to generate the subtracted spectra at all delays. The red line (repeated in the inset on an expanded vertical scale) shows an example of a subtracted spectrum at Δt = 1.28 ps). The contribution at BE >9.8 eV in the subtracted spectrum is due to ionization of $S_0^{\#}$ molecules to excited cationic states (see also Fig. 15), which are not included in the calculations presented in this work.

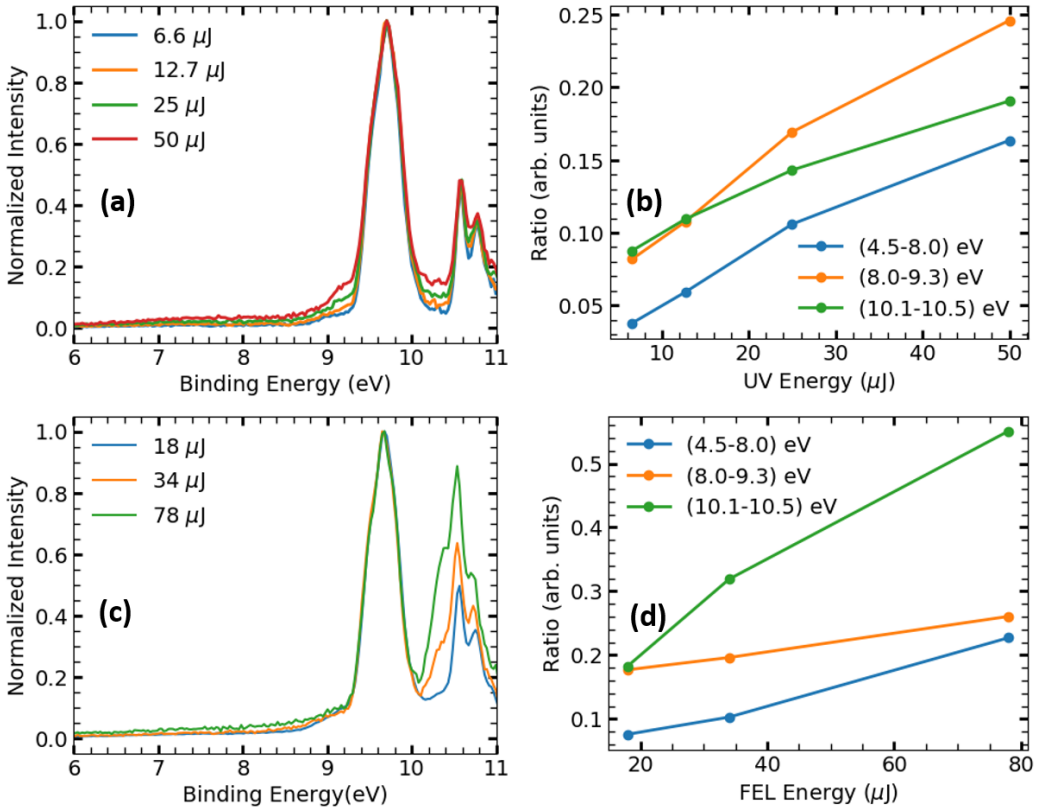

Figure 4: Pulse-energy dependence of the pump-probe signal. Dependence of the photoelectron spectra on the UV (a, b) and FEL (c, d) pulse energies. The latter are measured *before* the beamline optics and do not include the beamline transmission [*Svetina2015*]. The spectra in (a) and (c) are normalized with respect to the photoelectron signal intensity from unpumped molecules (BE ~9.6 eV). Panels (b) and (d) show the ratio of the photoelectron yield in the specified binding energy ranges with respect to the yield from unpumped molecules (BE 9.5-9.9 eV). The data shown in the manuscript were recorded at FEL and UV pulse energies of 19 μJ and 25 μJ, respectively.

2. Computational details

This section starts by providing additional details for the calculations of ionization potentials and surface hopping dynamics. We also provide additional benchmarks and supporting discussions relating to the calculations reported in the main text.

Ionization potentials for potential photoproducts and benchmarking: Ground-state geometry optimizations for thiophenone and its proposed photoproducts [*Murdock2014*] were conducted *in vacuo* at the MP2/6-311+G** level of theory, and the nature of all located stationary points was verified by harmonic vibrational frequency calculations. Based on these geometries, single-point electronic energy calculations were performed using MP2-F12/cc-pVDZ-F12 and CCSD(T)-F12/cc-pVDZ-F12 [*Kong2012, Hattig2012*]. Both methods are in good agreement for all the

computed ionization potentials of each molecule (see Section 2.8). All calculations were performed with Molpro 2012.

Trajectory surface hopping dynamics: The excited-state dynamics of thiophenone following photoexcitation were simulated using the mixed quantum/classical dynamics method trajectory surface hopping (TSH), employing the fewest-switches algorithm proposed by Tully [*Tully1990*]. The calculations were performed with the SHARC program package (v2.0) [*Mai2018*]. 46 initial conditions for the TSH dynamics were sampled stochastically from a Wigner distribution for uncoupled harmonic oscillators constructed from a frequency calculation at the ground-state optimized geometry of thiophenone. All trajectories were initiated in the bright S_2 state of thiophenone (see Section 2.4 for more information). The TSH dynamics employed a time step of 0.5 fs and SA(4)-CASSCF(10/8) for the electronic structure (benchmarking of this method is discussed more fully in Section 2.2) using Molpro 2012. The energy decoherence correction scheme by Granucci and Persico [*Granucci2007*] was applied to the electronic coefficients with the default constant of 0.1 hartree. Strict total energy conservation was ensured for each trajectory during the excited-state dynamics. However, the active space showed instabilities within a few tens of femtoseconds in the S_0 state. Such instabilities did not constitute an issue as the TSH dynamics were sufficiently stable to provide initial conditions for the subsequent ground-state AIMD calculations.

2.1. Characterization of the excited states

The electronic character of the first two excited singlet states of thiophenone at the Franck-Condon geometry was determined by natural difference orbitals (NDO), computed with the TheoDORE program (v 2.0) [*Plasser2014*].

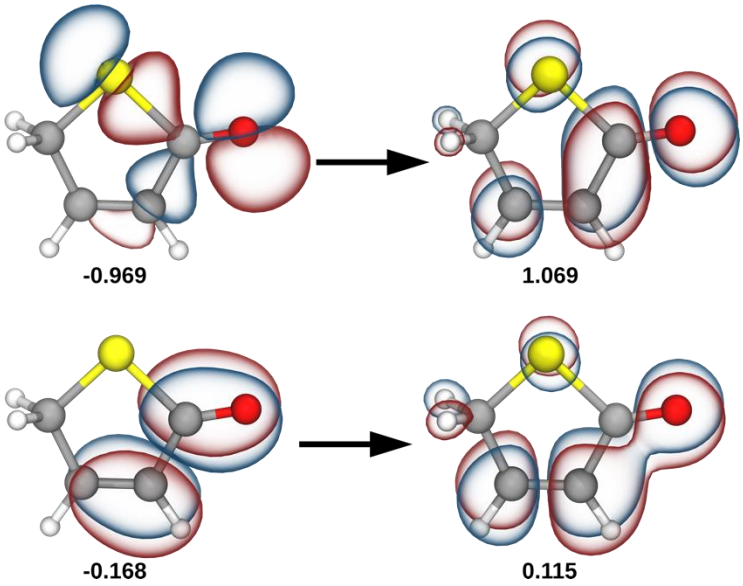

Figure 5: Electronic character of the S_1 state. Pairs of NDOs contributing to the S_1 state at the Franck-Condon geometry, with their respective eigenvalues.

Figures 5 and 6 show the NDOs (the eigenvectors of the difference density with respect to the ground electronic state) for the S_1 and S_2 states, respectively, with their corresponding eigenvalues; where negative (positive) eigenvalues describe the detachment (attachment) process. For detailed information about NDOs we refer to [*Plasser2014*]. The first pair of NDOs in Fig. 5 shows that the S_1 state is dominated by a $n(O)/\pi^*$ transition, with a small contribution of a π/π^* transition. The NDOs for the S_2 state (Fig. 6) encourage assignment as a $n(S)/\pi^*$ transition, but there is also a smaller but significant contribution from the $n(O)/\sigma^*$ transition (highlighting the dissociative character of this state) and a minor contribution from a π/π^* transition (similar to the small contribution in S_1).

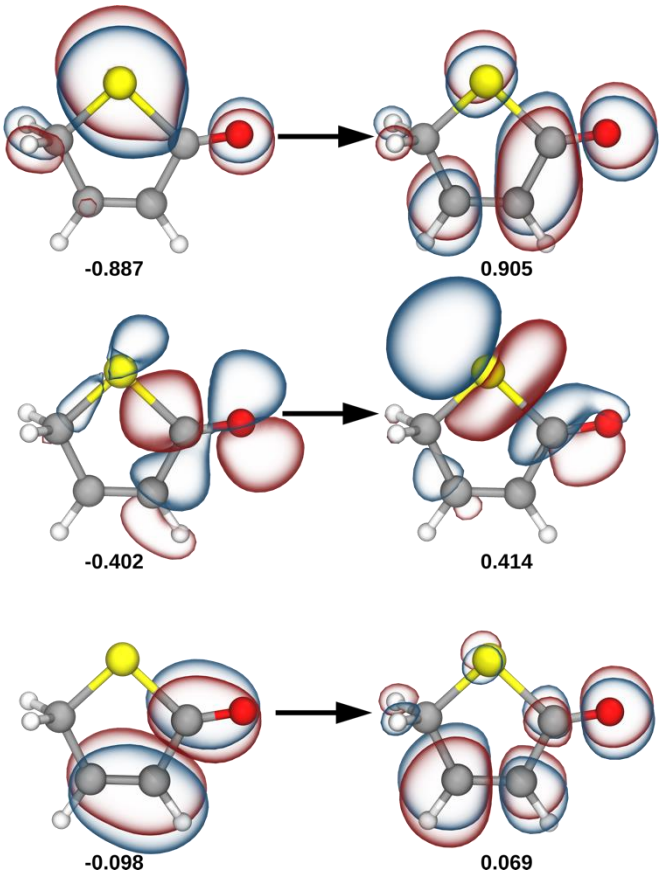

Figure 6: Electronic character of the S_2 state. Pairs of NDOs contributing to the S_2 state at the Franck-Condon geometry, with their respective eigenvalues.

2.2. LIIC pathways – validation of the electronic structure methods

LIIC pathways allow determination of the most straightforward path from geometry A to geometry B by interpolating a series of intermediate geometries (ten in the present work), using internal (not Cartesian) coordinates. It is important to recognize that *no reoptimization* is performed along these pathways. As a result, LIIC pathways should not be compared directly with minimum energy

paths, as the barriers observed in LIICs are upper estimates of the barriers that would be returned by locating the true transition states.

The LIIC pathways presented in the main text were derived from critical geometries optimized at the SA(4)-CASSCF(10/8) level of theory, but their energies were refined with XMS(4)-CASPT2(10/8). Figure 7 (right half) shows the same LIIC pathway calculated at the SA(4)-CASSCF(10/8) level. The overall shape of this pathway is in excellent agreement with that obtained using XMS(4)-CASPT2(10/8) (which is reproduced again in the right-hand part of Fig. 8 below), validating the use of SA-CASSCF for the nonadiabatic molecular dynamics. We note that the SA-CASSCF S_2/S_1 MECI point is not perfectly degenerate at the XMS-CASPT2 level of theory, while the S_1/S_0 MECI point is. The variations in ionization energy along the LIIC pathway as given by SA-CASSCF (shown at the top of Fig. 7) are also in excellent agreement with that returned by XMS-CASPT2.

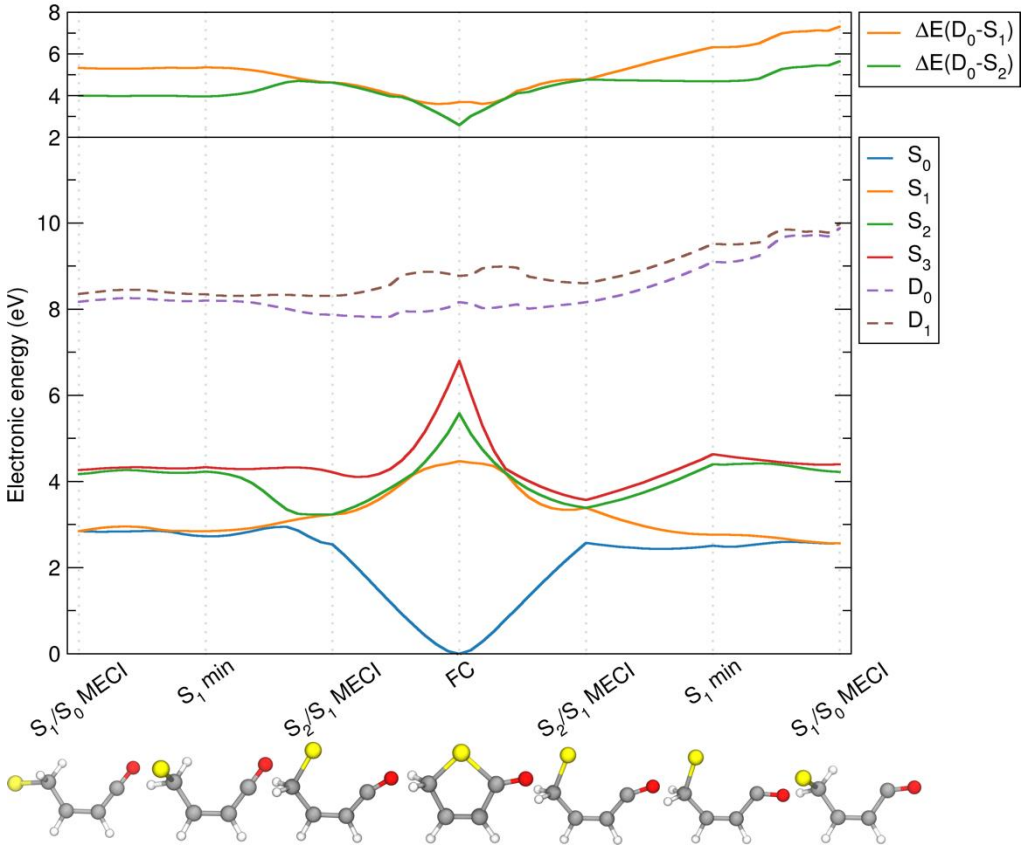

Figure 7: LIIC pathways. LIIC pathways computed at the SA(4)-CASSCF(10/8) (neutral thiophenone, solid lines) and SA(4)-CASSCF(9/8) (thiophenone cation, dashed lines) levels of theory. The LIIC pathway to the right of the FC region is that discussed in the main text, while that shown to the left is discussed below. Molecular geometries of the critical points located at the SA(4)-CASSCF(10/8) level of theory are represented beneath the figure.

The left part of Fig. 7 presents an alternative LIIC pathway connecting the FC point on the S_2 state to the S_0 state. This path differs in that the critical geometries located for the S_1 minimum and the S_1/S_0 MECI exhibit an out-of-plane configuration and a nonlinear C=C=O moiety (depicted at the appropriate points at the bottom of Fig. 7). The overall connectivity between S_2, S_1, and S_0 is nevertheless very similar to that observed for the LIIC pathway shown on the right: direct decay from the FC point on S_2 through conical intersections toward S_0. Importantly, the majority (76%) of the last S_1-to-S_0 hops observed during the TSH dynamics (discussed below) took place for molecular configurations similar to the S_1/S_0 MECI of the LIIC pathway on the right (*i.e.* the one presented in the main text). Figure 9 shows this comparison. We note the excellent agreement between the overall shape of this second LIIC pathway as determined by SA-CASSCF and XMS-CASPT2 methods (compare Figs. 7 and 8).

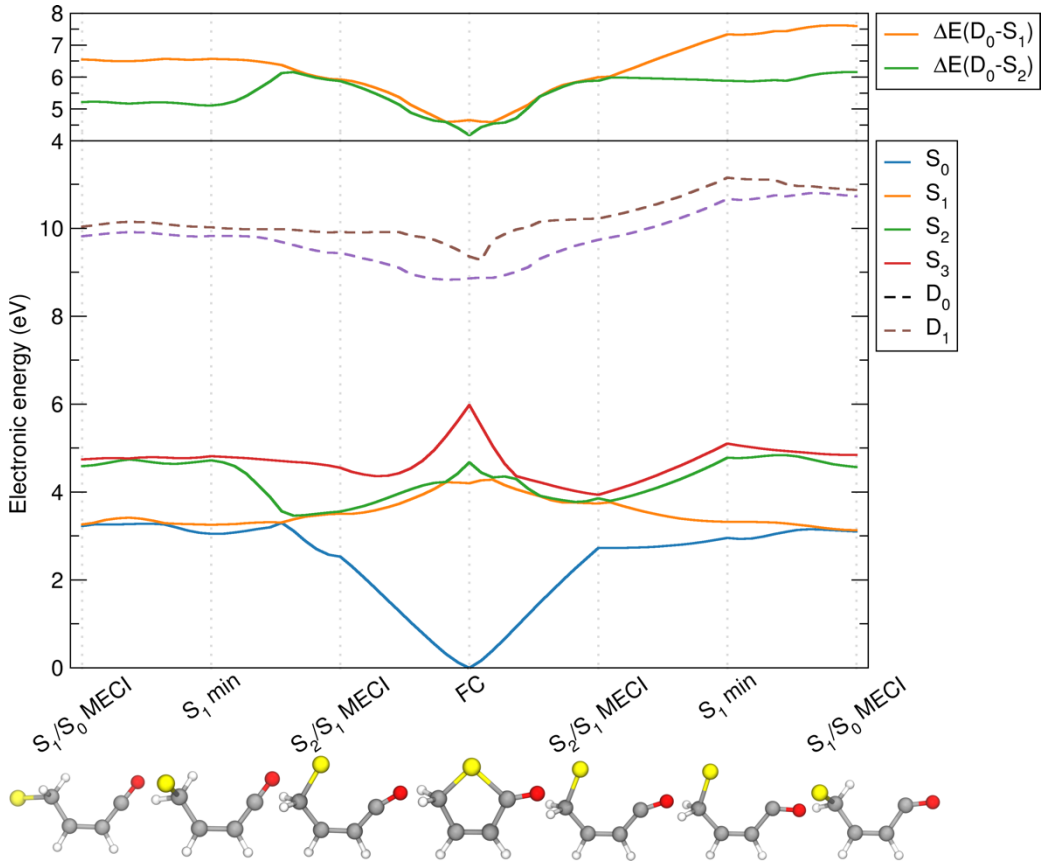

Figure 8: LIIC pathways with refined energies. LIICs pathways presented in Fig. 7 with energies refined at the XMS(4)-CASPT2(10/8) (neutral thiophenone, solid lines) and XMS(4)-CASPT2(9/8) (thiophenone cation, dashed lines) levels of theory. Molecular geometries of the critical points located at the SA(4)-CASSCF(10/8) level of theory are represented beneath the figure.

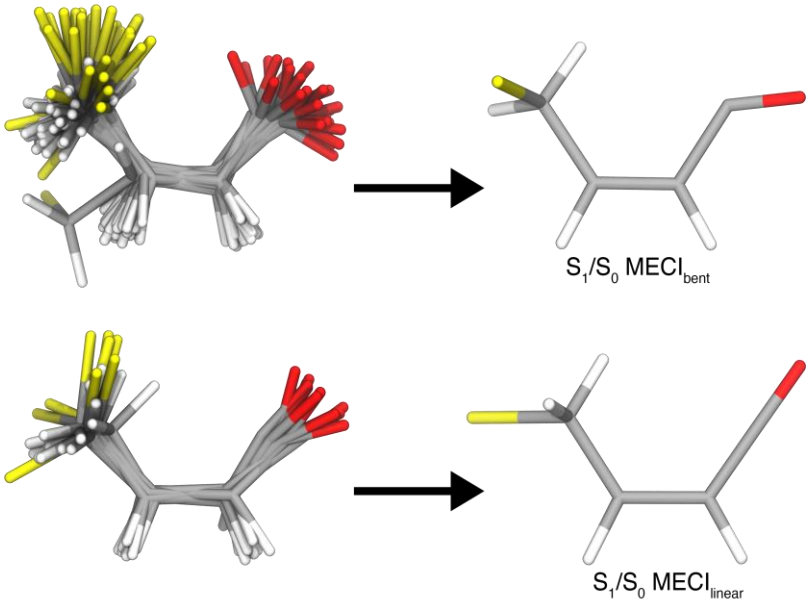

Figure 9: Geometries at the end of TSH calculations. Superimposed last S_1/S_0 hopping geometries from the TSH dynamics (shown on the left), grouped into two families according to whether the C=C=O angle corresponds to the bent MECI (76% of the hopping geometries, upper panel) or linear MECI (24% of the hopping geometries, lower panel).

Table 2 illustrates the influence of the choice of basis set on the XMS-CASPT2 calculations for the Franck-Condon geometry of thiophenone. At the SA-CASSCF level of theory, use of the larger cc-pVTZ basis set has negligible difference on the excitation energies for either neutral or charged thiophenone, and only a small, essentially rigid shift of all transitions energies is observed within XMS-CASPT2. Interestingly, the energy gap between the neutral and cationic states is increased when increasing the size of the basis set: for example, XMS-CASPT2/cc-pVTZ returns a IP_{vert} value for the $S_0 \rightarrow D_0$ ionization of 9.38 eV, *cf.* 8.94 eV for XMS-CASPT2/6-31G*. This accounts for the difference between the computed and measured BEs highlighted in the main text (inset of Fig. 3(a) in the main text). Nevertheless, we have used the smaller basis set to explore the PESs of thiophenone and for the TSH dynamics as a compromise between accuracy and efficiency and because the benchmarking assures us that this causes only a rigid energy shift.

Table 2: Illustration of the effect of the basis set on the electronic energies of thiophenone (at the Franck-Condon geometry). Energies are given in eV, with respect to the corresponding S_0 electronic energy.

Neutral	**SA(4)-CASSCF(10/8) 6-31G***	**SA4-CASSCF(10/8) cc-pVTZ**	**XMS(4)-CASPT2(10/8) 6-31G***	**XMS(4)-CASPT2(10/8) cc-pVTZ**
S_0	0	0	0	0
S_1	4.477	4.475	4.199	4.063
S_2	5.577	5.505	4.676	4.475
S_3	6.800	6.758	5.985	5.747
Cation	**SA(4)-CASSCF(9/8) 6-31G***	**SA4-CASSCF(9/8) cc-pVTZ**	**XMS(4)-CASPT2(9/8) 6-31G***	**XMS(4)-CASPT2(9/8) cc-pVTZ**
D_0	8.293	8.276	8.940	9.377
D_1	8.827	8.765	9.407	9.757

2.3 Selection rules for ionization from S_2 to D_0 and D_1

A key focus of the present study is the energetic separation between the neutral and cationic states of thiophenone along the LIIC pathway. Here it may be useful to introduce briefly an electronic argument for focusing the discussion on ionization to D_0 rather than to the D_1 state. The S_2 state has dominant n(S)/π* character in the Franck-Condon region (see Fig. 6). Importantly, the S atom lone pair remains the dominant donating orbital along the entire decay pathway, from the Franck-Condon point on S_2, to the S_2/S_1 MECI, and during the relaxation on S_1 towards S_1 min, eventually reaching the S_1/S_0 MECI. Similarly, the D_0 state is always formed by loss of an electron from the S atom lone pair along this LIIC pathway, whereas the D_1 state is initially (*i.e.* in the Franck-Condon region) characterized by removal of an electron from the O lone pair, before it too gains a larger contribution from the n(S) orbital towards the end of the LIIC (when the states get closer in energy). Simple ionization rules [*Arbelo-González2016*] suggest that ionization should be allowed from S_2 to D_0 along the entire LIIC pathway, as the two states differ by just a single spin-orbital (the accepting orbital in the excitation of the neutral). However, the same logic would imply that ionization from S_2 to D_1 is disfavored, as it necessitates (at least in the first part of the LIIC) a change of more than one spin-orbital in the ionization step.

2.4 Trajectory Surface Hopping dynamics of thiophenone

The electronic-state population trace obtained with TSH for 46 independent trajectories is shown in Fig. 3 of the main text. The trajectories were all initialized on the S_2 state, since the computed vertical transitions (at the SA(4)-CASSCF(10/8) level of theory) of 100 Wigner sampled structures indicate that this state is by far the 'brightest' when exciting from the S_0 state (see Fig. 10) and lies

at the appropriate energy for the chosen pump wavelength (when the transition energy is computed at the XMS-CASPT2 level of theory, see main text).

The populations depicted in the main text are computed as the fraction of trajectories evolving in a given electronic state at a given time. We note that the displayed population traces match well with those computed from the squares of the TSH electronic coefficients, averaged over all trajectories – indicating an internal consistency of the TSH algorithm. In accord with the LIIC pathways presented above, the nuclear wavepacket created on S_2 exhibits an ultrafast (<100 fs) decay towards the lower electronic states. The growth of the S_1 population, if fitted by a single exponential, is characterized by a waiting period of 19 fs and a growing time of 83 fs.

To shed light on the possible involvement of triplet states, we also investigated the effects of including two triplet states into the TSH dynamics. The TSH trajectories were initialized on S_2, as in the singlet-only TSH dynamics. The presence of triplet states was found not to influence the initial ring opening upon excitation. After internal conversion to the S_1 state, these triplet states become almost degenerate with the S_1 and S_0 states. By opening new decay channels, the presence of the triplet states could result in a slower decay to the ground state. In these test calculations, the population transfer to the triplet states was observed to be minor (<20% of the total electronic population). However, the instability encountered during the dynamics upon addition of triplet states in the SA-CASSCF calculations prevents us from drawing quantitative conclusions and these observations need to be regarded with due caution.

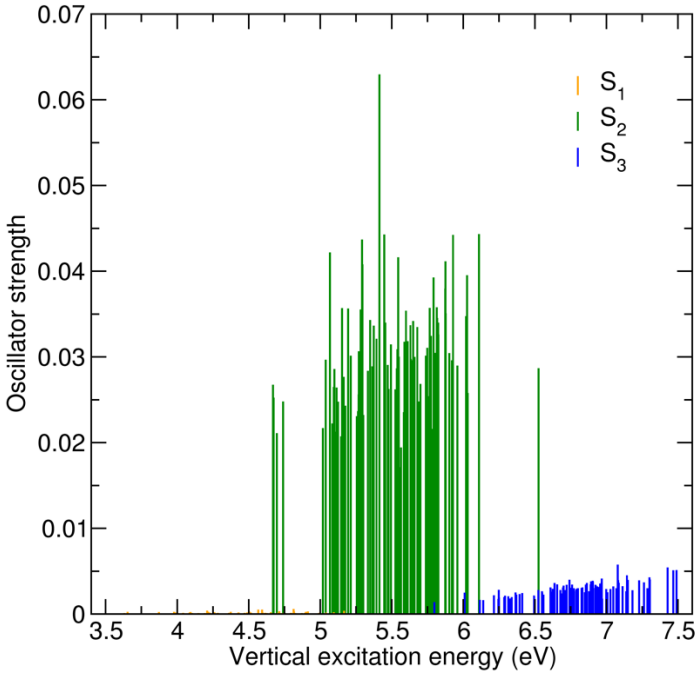

Figure 10: Oscillator strength of vertical transitions from the S_0 to the S_1, S_2, and S_3 states. Each stick represents a vertical excitation and corresponding oscillator strength for one of the 100 Wigner sampled molecular geometries, computed from the ground state to a given excited state (S_1, S_2, or S_3). Note that the contribution from S_1 between 4.5 and 5 eV is so small that it is barely visible in the figure.

2.5 Validation of the initial conditions for the ab initio molecular dynamics simulations

The AIMD simulations were initiated from the nuclear coordinates and with the momenta given by the TSH trajectories once they had reached the S_0 state and departed from the region of the S_1/S_0 MECI. Figure 11 shows two representative TSH trajectories (grey dots) reaching the ground state. The energy gap between the S_0 and S_1 states increases shortly after the TSH trajectory hopped to S_0, offering a validation for the approximation that the subsequent dynamics on S_0 will be considered as adiabatic, *i.e.*, within the Born-Oppenheimer approximation. The percentages in Fig. 11 indicate the contribution of the closed-shell ground-state configuration to the S_0 electronic wavefunction for different molecular geometries selected along each trajectory (each such geometry is indicated by a cross). This percentage increases rapidly when the TSH trajectory is driven by the S_0 PES. The arrows in Fig. 11 indicate the points selected to initialize the AIMD simulations – the nuclear coordinates and velocities obtained from the TSH trajectory were used to initiate the AIMD.

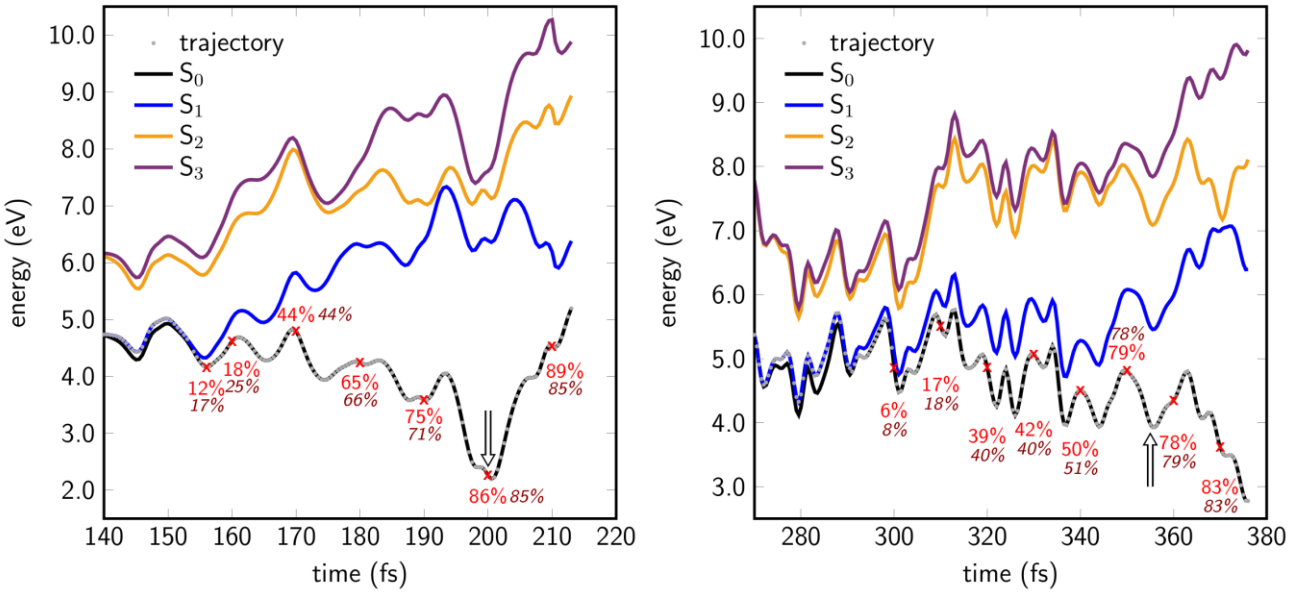

Figure 11: Electronic energies along two different TSH trajectories. The dotted line indicates the electronic state driving the TSH dynamics at a given time. The percentages give the contribution of the closed-shell ground-state configuration to the S_0 electronic wavefunction (values determined at the SA(4)-CASSCF(10/8) and XMS(4)-CASPT2(10/8) levels of theory are shown in red and in burgundy (italic), respectively) at a given geometry (highlighted by a cross). The arrows show the points used to initiate the subsequent AIMD on S_0.

2.6 AIMD trajectories out to t = 2 ps and a trajectory exhibiting interconversion between different photoproducts

One focus of the present work was to determine the distribution of the IP_{vert} values for the $S_0 \rightarrow D_0$ transitions of thiophenone and its photoproducts; possible consequences of the energetic proximity of D_1 are considered in section S2.9. Each AIMD trajectory starts from a slightly different time (defined relative to the initial photoexcitation process), since the TSH trajectories reach the S_0 state at different times. Defining a time-average of the IP_{vert} values over all trajectories is thus challenging, but this does not preclude investigation of the narrowness of the BE distribution observed at later Δt (*i.e.* following non-radiative decay to the S_0 state) as shown in Fig. 4 of the main text.

Figure 12 shows the IP_{vert} values calculated along an AIMD trajectory in the S_0 state, chosen as it shows interconversion between three photoproducts: 2-(2-thiiranyl)ketene (P3), thiophenone, and 2-(2-sulfanylethyl)ketene (P2); the molecular structures are shown below. The IP_{vert} value is computed every 10 fs along the trajectory, and the orange line shows a running average of IP_{vert} over 10 time steps. As with the histograms presented in Fig. 4 of the main text, this plot serves to highlight the similar IP_{vert} values of the different photoproduct configurations (apart from thiophenone itself, which exhibits a slightly higher IP_{vert} value). In all AIMD simulations, compounds were identified based on characteristic atomic connectivities determined by measuring bond lengths or angles, as depicted in Fig. 13.

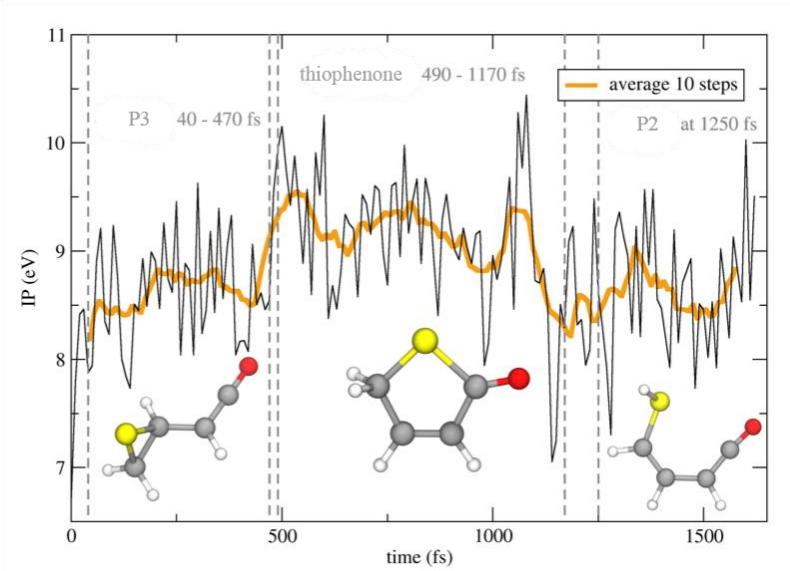

Figure 12: Vertical ionization potential value along an example AIMD trajectory on S_0.

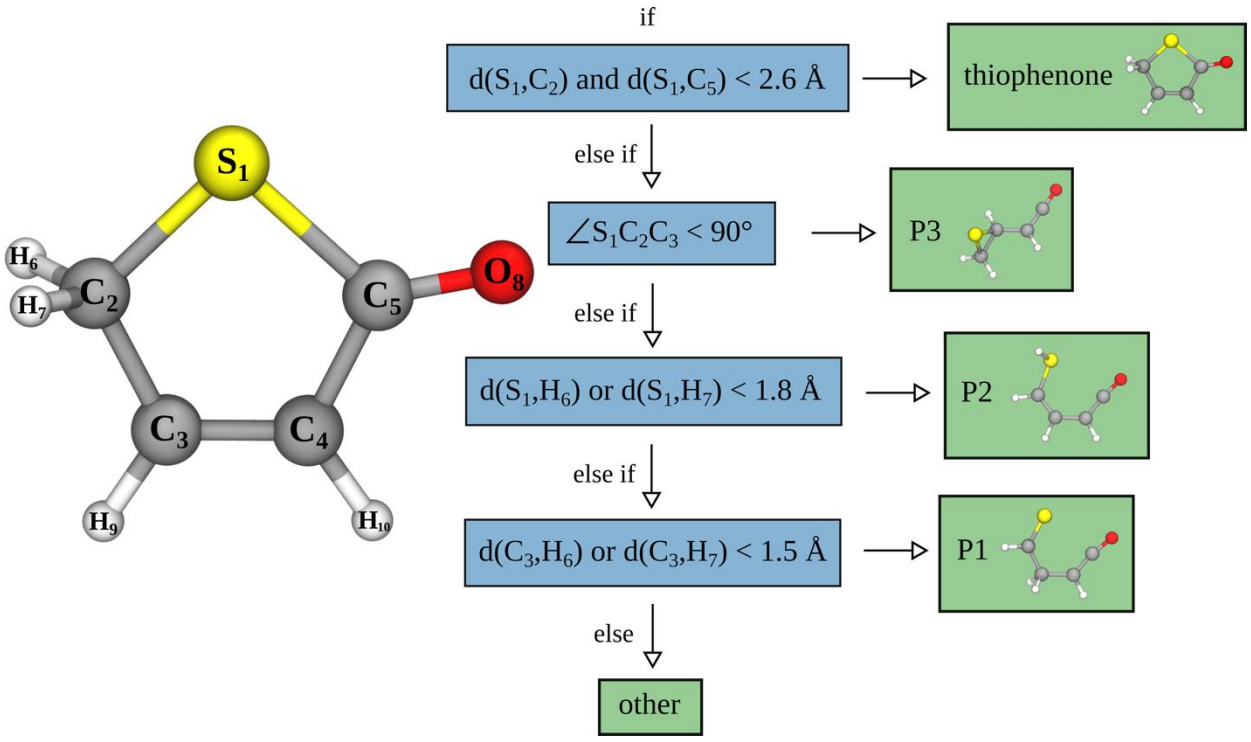

Figure 13: Decision tree for the identification of photoproducts during the AIMD.

2.7 Normal distribution of IPs

The histogram of the IP data computed along all AIMD trajectories (without distinguishing the photoproduct) was fitted to a normal distribution, as shown in Fig. 14. The resulting mean value was 8.93 eV with a standard deviation σ = 0.41 eV. The FWHM was calculated from the standard deviation according to $FWHM = 2\sqrt{2\ln(2)}\,\sigma$.

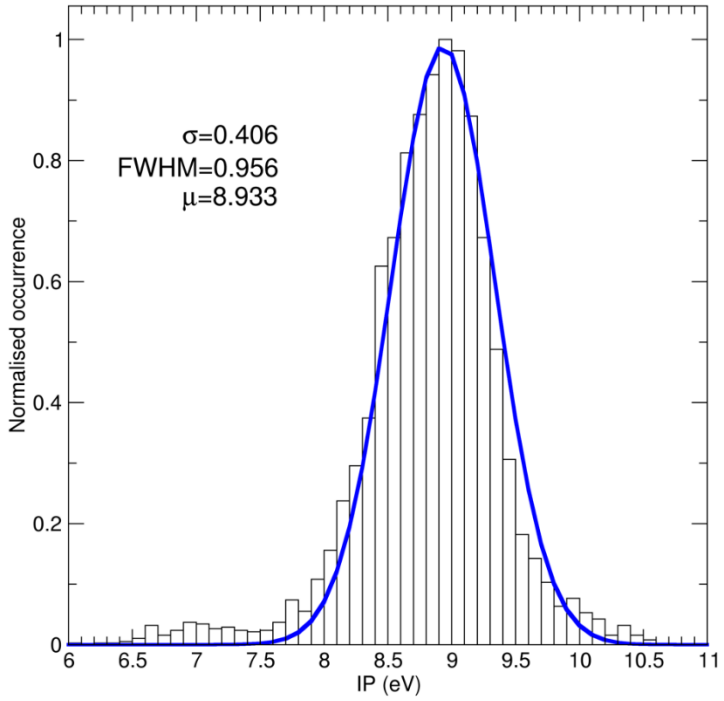

Figure 14: Histogram of IPs computed along the AIMD trajectories and their fit to a normal distribution.

2.8 Validation of the methodology to compute ionization potentials between S_0 and D_0

Table 3 illustrates the close agreement between the IP values computed with CCSD(T)-F12/cc-pVDZ-F12 and MP2-F12/cc-pVDZ-F12 for different possible photoproducts of thiophenone. All geometries for these benchmarking calculations were optimized at the MP2/6-311+G** level of theory. The table also shows energy differences between the electronic ground state energy of the photoproduct and the parent thiophenone molecule. Convergence of the CCSD(T)-F12 and MP2-F12 results with respect to basis set size has been tested by comparing the results obtained with cc-pVDZ-F12 and cc-pVTZ-F12 for thiophenone and for the P3 isomer. Only minor differences were observed between the two basis sets: for thiophenone, the variation in IPs between the two basis sets was 0.05 eV (CCSD(T)-F12) and 0.02 eV (MP2-F12). The level of agreement observed between CCSD(T)-F12 and MP2-F12 for IPs and the convergence observed for both methods with the cc-pVDZ-F12 basis validate the use of MP2-F12/cc-pVDZ-F12 for the results presented in the main text.

Note that the present calculations use a *vertical* approximation to derive the S_0–D_0 energy gap, *i.e.*, we do not use the lowest energy point on the cation PES, but the point of the cationic PES

corresponding to the particular nuclear arrangement in the (neutral) ground state. Both the number of configurations sampled (>4000) and the conformational flexibility of the photoproducts would challenge an estimation of the vibrational overlap based on the harmonic approximation (as is commonly employed).

It is also worth commenting on the possible role of other cationic states during the AIMD process, particularly D_1. The analysis presented here was limited to the distribution of the lowest IP band (*i.e.* $S_0^{\#}$ to D_0) during the athermal dynamics following the nonadiabatic relaxation to the ground state. As expected from the LIICs presented above, the D_1 cationic state is expected to be only slightly higher in energy than D_0. To gain some estimate of the influence of D_1 on the high energy side of the IP distribution (*i.e.* of any broadening due to D_1), the D_1–D_0 energy splitting was computed (using XMS(2)-CASPT2(9/8)) for the three photoproducts observed during the AIMD, at their optimized ground state energy. The D_1–D_0 energy gaps derived in this way are only 0.324 eV (for P1), 1.537 eV (for P2) and 0.493 eV (for P3), suggesting that proper inclusion of the D_1 state would likely affect the high energy side of the computed IP distributions.

Table 3: Ionization potential of thiophenone and photoproducts. Comparison between CCSD(T)-F12 and MP2-F12 calculated values of the IPs of different photoproducts and of their electronic energies relative to that of the S_0 state of thiophenone.

	thiophenone	P1	P2	P3	P4	P5	P6
	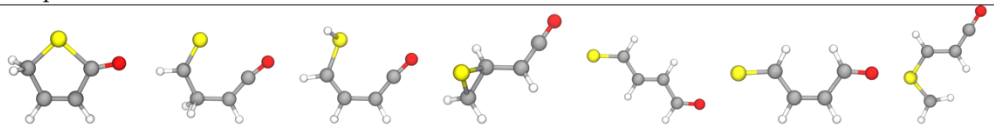						
CCSD(T)-F12							
IP / eV	9.663	9.177	8.310	8.796	9.206	9.223	7.272
relative to thiophenone							
ΔS_0 / eV		1.549	1.410	1.455	1.274	1.396	2.878
Δ IP / eV		-0.486	-1.353	-0.867	-0.458	-0.440	-2.391
MP2-F12							
IP / eV	9.799	9.362	8.368	8.668	9.374	9.392	7.566
relative to thiophenone							
ΔS_0 / eV		1.567	1.417	1.367	1.386	1.512	2.761
Δ IP / eV		-0.436	-1.431	-1.130	-0.425	-0.407	-2.233

Finally, the chosen computational strategy for estimating photoelectron spectra was benchmarked by comparing the measured (He I) photoelectron spectrum of thiophenone with that computed using configurations extracted from a ground-state AIMD initiated from a set of nuclear coordinates and momenta sampled from a Wigner distribution (spectrum labelled ‘cold’ in Fig. 15). Figure 15 also compares the photoelectron spectrum computed for this ‘cold’ thiophenone sample with that obtained for $S_0^{\#}$ thiophenone molecules (*i.e.* molecules that have undergone photoexcitation and subsequent non-adiabatic coupling to the S_0 PES, labeled ‘hot’).

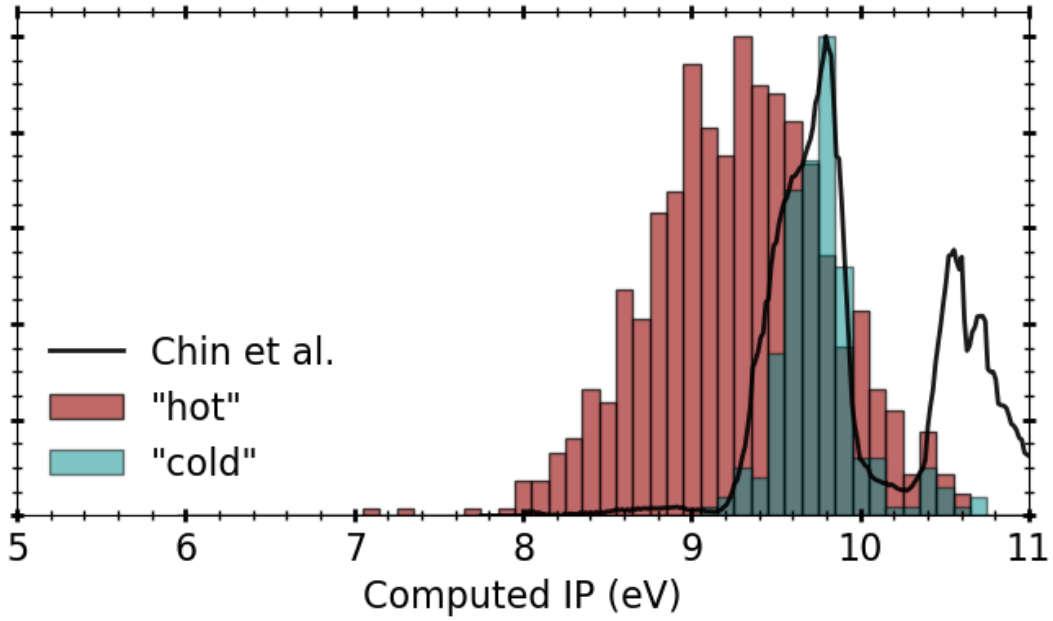

Figure 15: Comparison of measured (He I) photoelectron spectrum of thiophenone (Chin *et al.*, 1998, solid black trace) and the distributions of computed $S_0 \rightarrow D_0$ IP_{vert} values for 'cold' (turquoise) and 'hot' (burgundy) thiophenone molecules. The former histogram, obtained from AIMD simulations of S_0 molecules with internal energy equal to the zero-point energy only, has been scaled vertically to match the experimental spectrum and illustrates the good agreement with the experimental IP. The latter histogram, which shows the distribution of IP_{vert} values associated with closed-ring 'hot' thiophenone species (computed at the MP2/cc-pVDZ-F12 level of theory) produced after photoexcitation and subsequent relaxation, has been scaled to have the same maximum. Note that the present theory has not attempted to model the $S_0 \rightarrow D_2$ ionization responsible for the BE >10.4 eV peak in the experimental spectrum.

2.9 Nature of the ionization process

For the electrons identified as being involved in the ionization process, spin densities were computed (at the MP2/cc-pVDZ level of theory) for the optimized structures of the molecules observed during the AIMD; thiophenone, and the ketene photoproducts P1, P2 and P3 observed in the AIMD calculations.

Figure 16 shows the spin densities plotted with an isosurface of 0.02. The spin densities are shown in blue (the green isosurface shows the negative contributions and offers a measure of spin contamination). The spin densities for thiophenone, P1 and P3 are mainly located on the sulfur atom, consistent with the previous conclusion that ionization occurs mainly from the *n*(S) orbital. In the case of P2 (bottom right structure in Fig. 16), the spin density is mostly on the C=C double bond, suggesting that ionization occurs from this π orbital. However, we note that the optimized geometry of the P2 structure may not be fully representative of the hot ground-state photoproduct. For the other photoproducts, the histograms of IPs calculated for the structures observed during the AIMD are all centered at the IP value calculated for the optimized point. For P2, the calculated IP at the optimized point is 8.37 eV, whereas the histogram of IPs of the hot photoproduct is

centered at ~8.7 eV. Additionally, the distribution of IPs for P2 is broader than that for any of the other structures. To this end, spin densities were computed for the frames of an AIMD trajectory showing formation of P2. We observe that, for such $S_0^{\#}$ geometries, the spin density is localized not only around the C=C bond but also on the sulfur atom. Thus we conclude that the shift to a higher IP and the broadening of the IP distribution during the AIMD (*cf*. the IP obtained from the ground-state optimized structure) can be understood if we assume that ionization to form D_0 occurs from the π and the *n*(S) orbitals. Finally, we note that the characters of the D_0 photoproducts accord with that observed in the previously discussed XMS(2)-CASPT2(9/8) calculations.

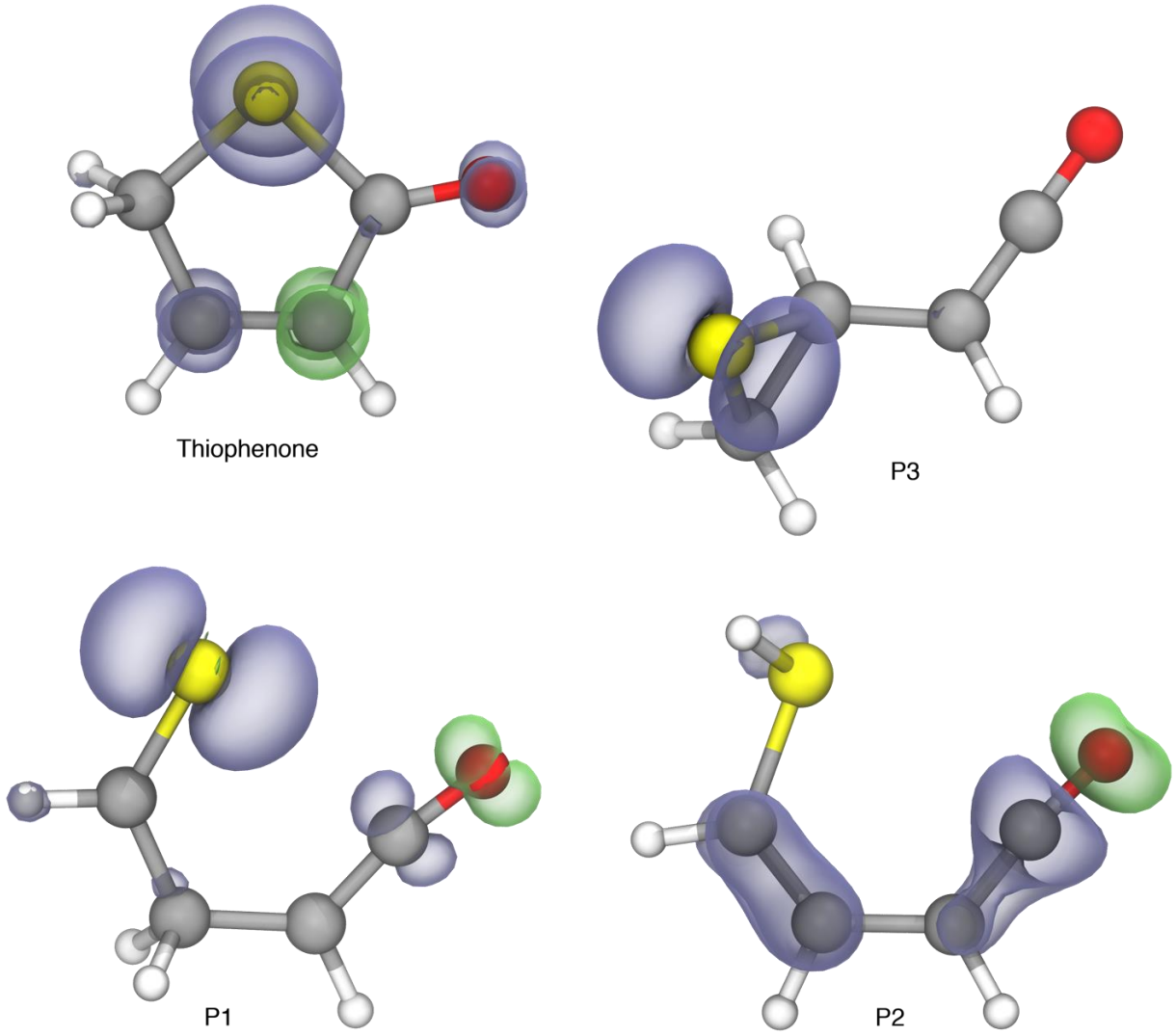

Figure 16: Spin densities of thiophenone and photoproducts. Spin densities (blue) of the optimized structures of the photoproducts observed, and their negative contributions (green).

2.10 AIMD trajectories out to t = 100 ps and trajectories exhibiting dissociation to CO + thioacrolein

To explore the possible evolution of the ground state photoproducts over longer timescales, 10 AIMD trajectories (out of the initial 22) were propagated until t = 100 ps. Issues of particular interest here were (i) whether the 'hot' $S_0^{\#}$ thiophenone photoproducts would eventually ring-open, and (ii) whether the primary photoproducts might undergo further fragmentation. At the start of the long-time AIMD simulations (*i.e.*, at t = 2 ps), the chosen pool of 10 molecules involved 4 (*i.e.* 40%) with 'hot' thiophenone structures, 4 P1 and 2 P2 structures. We stress that these proportions were chosen solely for the purpose of investigating the possible fate of some specific photoproducts (particularly 'hot' thiophenone) during the long-time exploratory AIMD; they do not reflect the relative photoproduct yields after t = 2 ps (recall Fig. 4 in the main paper). Figure 17 shows how these photoproduct proportions evolve over the full length of the AIMD. These (admittedly small number of) trajectories show the population of thiophenone decreasing and new dissociation products (thioacrolein + CO) arising from decay of both 'hot' thiophenone and photoproduct P1. The computed S_0–D_0 IP_{vert} value for thioacrolein (9.04 and 8.99 eV for the Z- and E-isomers, respectively, at the MP2-F12/cc-pVDZ-F12 level of theory) is in very good agreement with the experimental value [*Bock1982*]. Clearly, the present long time AIMD analysis is statistically limited, but it serves to highlight possible pathways that can alter the composition of the photoproducts formed on the S_0 PES over time in a manner that could account for the long time variation in the TRPES signal observed in the range $8 \leq BE \leq 9.5$ eV (Fig. 4(a) in the main text).

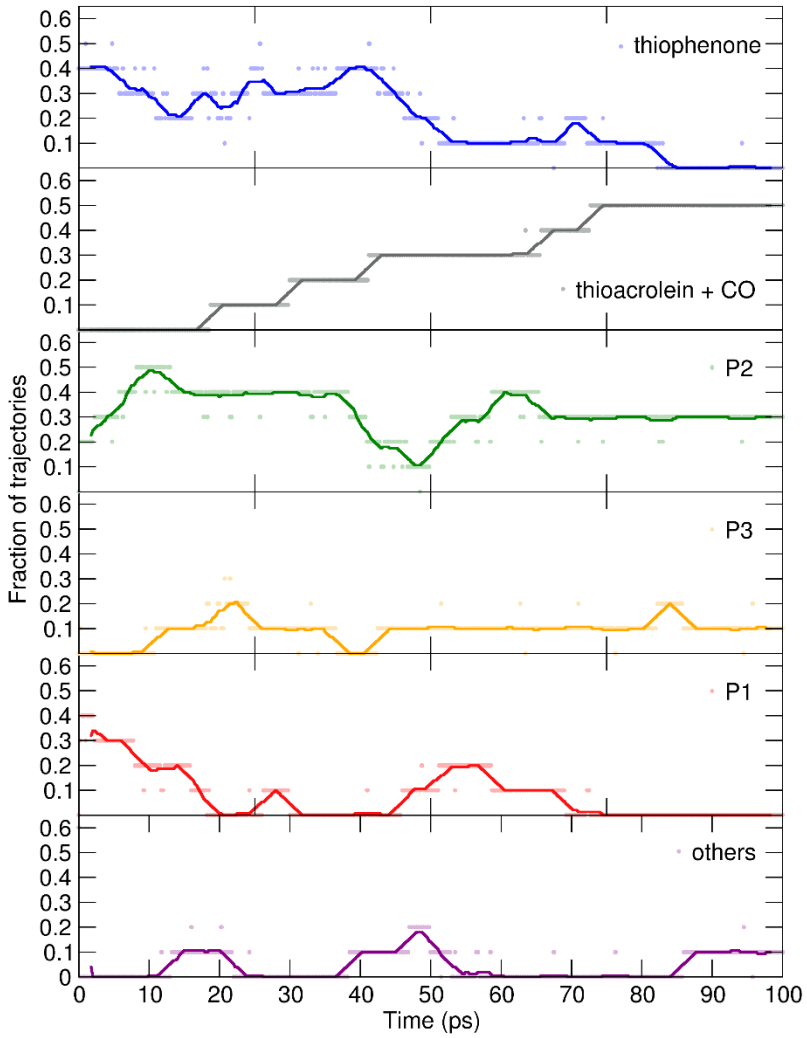

Figure 17: Photoproduct distribution during the long-time AIMD simulations. The dots indicate the proportion of a given photoproduct sampled every 0.25 ps, while the solid lines show the corresponding running average (over 15 time steps).

Supplementary References:

Arbelo-González, W., Crespo-Otero, R., & Barbatti, M. Steady and time-resolved photoelectron spectra based on nuclear ensembles. *Journal of Chemical Theory and Computation* **12**, 5037-5049 (2016).

Bock, H., Mohmand, S., Hirabayashi, T. & Semkow, A. Gas-phase reactions. 29. Thioacrolein. *J. Am. Chem. Soc.* **104**, 312-313 (1982).

Chin, W.S. et al. He I and He II photoelectron spectra of thiophenones. *J. Electron Spectroscopy Related Phenomena* **88–91**, 97–101 (1998).

Granucci, G. & Persico, M. Critical appraisal of the fewest switches algorithm for surface hopping. *J. Chem. Phys*. **126**, 134114 (2007).

Hattig, C., Klopper, W., Köhn, A. & Tew, D.P. Explicitly Correlated Electrons in Molecules. *Chem. Rev*. **112**, 4−74 (2012).

Kong, L., Bischoff, F.A. & Valeev, E.F. Explicitly Correlated R12/F12 Methods for Electronic Structure. *Chem. Rev.* **112**, 75− 107 (2012).

Mai, S., Marquetand, P. & González, L. Nonadiabatic dynamics: the SHARC approach. *WIREs Comput. Mol. Sci*. **8**, 6-e1370 (2018).

Mai, S. et al. SHARC2.0: Surface Hopping Including Arbitrary Couplings — Program Package for Non-Adiabatic Dynamics, *sharc-md.org*, 2018.

Plasser, F. TheoDORE 2.0: a package for theoretical density, orbital relaxation, and exciton analysis. *Available from http://theodore-qc.sourceforge.netF*.

Plasser, F., Wormit, M., Dreuw, A. New tools for the systematic analysis and visualization of electronic excitations. I. Formalism. *J. Chem. Phys.* **141**, 024106 (2014).

Svetina, C. et al. The Low Density Matter (LDM) beamline at FERMI: optical layout and first commissioning. *J. Synchrotron Rad.* **22**, 538–543 (2015).

Tully, J.C. Molecular dynamics with electronic transitions. *J. Chem. Phys.* **93**, 1061–1071 (1990).